Tracking upper tropospheric water vapor radiances: A satellite perspective

Brian J. Soden

Geophysical Fluid Dynamics Laboratory/NOAA, Princeton, New Jersey

Abstract. Hourly observations of 6.7 μm "water vapor" radiances from geostationary satellites are used in conjunction with an objective pattern-tracking algorithm to trace upper tropospheric water vapor features from sequential images. Analysis of measurements covering the 3 month period of June-August 1987 illustrates a close relationship between the upper tropospheric moisture and the tropical circulation. Over humid tropical regions the movement of water vapor patterns reveals a diverging upper level flow away from centers of deep convection. Likewise, arid subtropical regions are characterized by converging upper level water vapor patterns indicating sinking air. The evolution of upper tropospheric moisture is also explored from a Lagrangian perspective by considering the change in moisture of a pattern as it is tracked from one image to the next. This analysis reveals that the clear-sky upper troposphere in both tropical and subtropical regions becomes increasingly drier with time reflecting the impact of large-scale subsidence in drying the troposphere. When separated according to cloud amount, water vapor patterns associated with clouds are observed to dry substantially slower than those without clouds, presumably due to the evaporation of cloud condensate. Trajectories of upper tropospheric moisture are also constructed by iteratively tracking water vapor patterns from successive satellite images. The trajectories reveal two distinct paths for water vapor patterns entering the dry subsidence region of the subtropical South Pacific. One path highlights the southward propagation of convective outflow from the tropics while the other path reflects the injection of moisture from eastward propagating subtropical disturbances. The existence of two distinct source regions suggests that a complete picture of the processes regulating the driest and most radiatively transparent regions of the subtropics will require an understanding of both types of convective systems.

1. Introduction

Water vapor is widely recognized to be a key component of the climate system. The importance of water vapor, both as a greenhouse gas and as a feedback mechanism, underscores the need for an accurate understanding of the processes that control it. Water vapor associated with large-scale subsidence in the subtropical trade belts is particularly important due to its low relative humidity. Since the outgoing longwave radiation is most sensitive to humidity fluctuations at low values [*Thompson and Warren*, 1982; *Spencer and Braswell*, 1997] small changes in subtropical moisture, particularly in the middle to upper troposphere, can have large effects on the radiative energy balance. Recent studies have emphasized the importance of the tropical circulation in determining the moisture content and outgoing longwave radiation of the tropics [e.g., *Sun and Lindzen*, 1993; *Stephens et al.*, 1993 *Soden and Fu*, 1995; *Schmetz et al.*, 1995a; *Bates et al.*, 1996; *Sherwood*, 1996a, b; *Sun and Held*, 1996; *Stephens et al.*, 1996; *Salathe and Hartmann*, 1997; *Soden*, 1997; *Spencer and Braswell*, 1997]. The interaction between the tropical circulation and subtropical moisture also plays a key role in regulating the dynamics of the tropical climate [*Pierrehumbert*, 1995].

Despite the importance of water vapor in climate, the role of dynamical processes such as convection and subsidence in controlling the moisture content of the middle to upper troposphere are not well understood. Much of the uncertainty surrounding the moisture budget of the upper troposphere reflects the lack of suitable observations, particularly over data sparse regions of the tropics. An alternative to conventional observations are water vapor and wind measurements derived from geostationary satellite images [e.g., *Schmetz et al.*, 1995a; *Jedlovec*, 1997; *Velden et al.*, 1997]. The high spatial and temporal sampling afforded by geostationary satellites provides a unique opportunity to track the movement and evolution of water vapor structures on hourly time-scales. This investigation demonstrates the applicability of high temporal resolution geostationary measurements for better understanding the processes affecting the moisture content of the upper troposphere. Specifically, archived observations of hourly 6.7 μm "water vapor" radiances from the GOES Pathfinder project are used in conjunction with an objective pattern-tracking algorithm to follow water vapor features from sequential time-lapsed satellite imagery. From this analysis, climatological diagnostics relating to the moisture distribution and large-scale tropical circulation of the upper troposphere are derived. The temporal evolution of the upper tropospheric moisture field is also described from a Lagrangian perspective. The Lagrangian analysis is useful for identifying pattern trajectories associated with tropical convection and subtropical sub-

sidence as well as for describing the growth and decay of moisture associated with these processes. This information is used to investigate the following basic questions regarding the role of convection and subsidence in regulating upper tropospheric moisture:

Where does moisture expelled from convective regions go?
Where does moisture entering the dry subtropics originate?
How does the moisture field evolve during these processes?

Section 2 describes the satellite data and methodology used for obtaining upper tropospheric relative humidity (UTH) and water vapor pattern displacement vectors (PDVs) from the satellite imagery. Section 3 presents the time-mean distribution of the upper tropospheric moisture and circulation fields for JJA 1987. In section 4 the growth and decay of the UTH field is considered from a Lagrangian perspective and related to the vertical motion of upper tropospheric air. In section 5, water vapor radiance patterns are tracked over several successive images to construct pattern trajectories and characterize the evolution of the moisture field along these trajectories. A summary of the results is presented in section 6.

2. Tracking GOES Water Vapor Radiances

2.1. Upper Tropospheric Relative Humidity

Hourly observations of the 6.7 μm brightness temperature ($T_{6.7}$) are obtained from GOES-7 for the 3-month period June, July, August 1987. The 6.7 μm channel is located near the center of a strong water vapor absorption band and under clear skies is primarily sensitive to the relative humidity averaged over a deep layer centered in the upper troposphere [*Soden and Bretherton*, 1993]. This layer typically extends from ~200-500 hPa and shifts vertically depending upon the nature of the atmosphere, moving to slightly lower altitudes for cold-dry profiles and slightly higher altitudes for warm-moist profiles. *Soden and Bretherton* [1993] (hereinafter referred to as SB93) presented an analytic expression, based upon simplified radiative theory, to relate the clear-sky $T_{6.7}$ to relative humidity. Following SB93, a vertically averaged upper tropospheric relative humidity (UTH) is obtained from the clear-sky $T_{6.7}$ according to

$$\ln\left(\frac{\text{UTH }p_o}{\cos\theta}\right) = a + bT_{6.7} \tag{1}$$

where a and b are empirically determined coefficients, θ is the satellite zenith angle, and p_0 is a normalized base pressure. The quantity UTH is defined as the weighting-function-averaged relative humidity computed over a deep layer of the upper troposphere (roughly 200-500 hPa; see SB93). The p_0 term is obtained from a monthly mean climatology, as described by *Soden and Bretherton* [1996] and accounts for latitudinal and seasonal changes in atmospheric temperature on the clear-sky $T_{6.7}$. The effect of daily variations in p_0 on UTH is typically much smaller than the instrument noise in the 6.7 μm channel and is therefore neglected.

The coefficients a and b are determined by tuning the relationship in equation (1) to detailed radiative transfer calculations. A series of radiance computations are made using temperature and moisture profiles from ECMWF analyses as input to the CIMSS (Cooperative Institute for Meteorological Satellite Studies) transmittance model. The CIMSS model is a 40 level multivariate regression model based upon FASCODE line-by-line transmittance model calculations. The formulation of the CIMSS model is similar to that described by *Eyre*
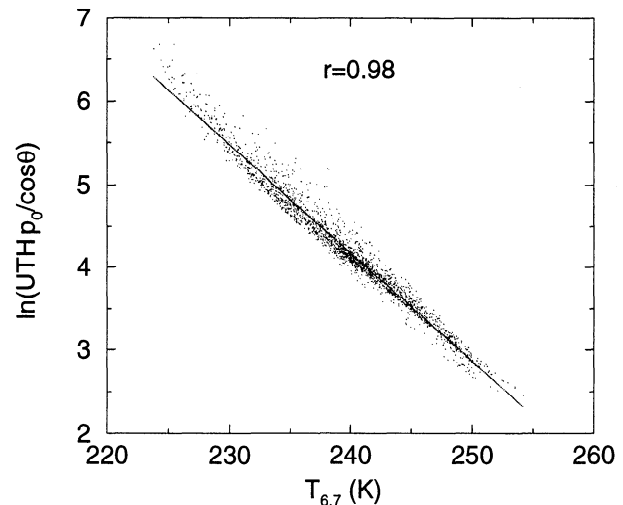

Figure 1. Scatterplot of the forward-calculated $T_{6.7}$ versus the corresponding value of $\ln(UTH\,p_o)/(\cos\theta)$. The solid line represents a linear, least squares regression.

[1991]. The CIMSS forward radiance calculations are specific to a particular satellite, thus the coefficients obtained here correspond specifically to the 6.7 μm channel spectral response function on the GOES 7 satellite. The temperature and moisture profiles are taken from the July 1, 1987, ECMWF analyses using all profiles located within the GOES viewing domain. Forward radiance calculations are then performed to determine the value of $T_{6.7}$ which would be observed by the satellite under those conditions. The forward-calculated $T_{6.7}$ are then compared to the vertically-averaged upper tropospheric relative humidity with respect to ice computed explicitly from the same moisture profile (using the weights listed in Table 2 of SB93). The results of this procedure are presented in Figure 1. Linear regression (shown as the solid line in Figure 1) of $T_{6.7}$ versus $\ln(UTH\,p_o)/(\cos\theta)$ is then used to determine the coefficients in equation (1), which in this case are $a=35.5$ and $b=-0.130$ K^{-1}. These coefficients are slightly different from those presented by SB93, because that study did not account for the effect of variations in base pressure (p_o) on the $T_{6.7}$ (see SB96 for a further discussion of this effect).

It is important to note that the sample profiles used to tune equation (1) are representative of a wide range of geographic and synoptic conditions. Thus while the precise values of the coefficients may depend upon the details of the "training" profiles, the resulting UTH climatology is relatively insensitive to this process. For example, SB96 derived coefficients (for the TOVS 6.7 μm channel) using training profiles from different operational forecast models as well as from radiosonde measurements. The resulting UTH climatologies were shown to be very insensitive to the choice of the sample profile data set. Here we extend this sensitivity analysis by showing that the UTH product is also insensitive to seasonal or regional variations in the training profiles. Table 1 lists the coefficients obtained using ECMWF temperature and moisture profiles corresponding to three other seasons (January, April, and October). Coefficients were determined as described above using temperature and moisture profiles from the first day of each month to represent the effects of seasonal differences in moisture and temperature profiles on the retrieval. The UTH derived from these coefficients was compared to that obtained using the July coefficients ($a=35.5$, $b=-0.130$ K$^-$

Table 1. Sensitivity of UTH Retrieval to Seasonal Variations in Training Profiles.

Month	a	b, K^{-1}	rms	Bias	Corr.
July	35.5	-0.130	0.0	0.0	1.0
Oct.	36.8	-0.135	6.4	-5.1	> 0.99
Jan.	34.9	-0.127	6.5	-5.7	> 0.99
April	36.7	-0.135	1.1	0.3	> 0.99

The values of the regression coefficients (a, b) obtained using ECMWF profiles from the first day of four different months are shown. To evaluate its sensitivity, the UTH is determined from one day of GOES $T_{6.7}$ observations using each set of coefficients. The rms difference (in %), bias (in %), and spatial correlation of each UTH estimate is then compared to that obtained from the July coefficients.

[1]) and the results (rms difference, bias, and correlation) summarized in Table 1. Note that while the coefficients may differ, the retrieved UTH is relatively insensitive. In all cases the bias and rms difference in UTH is less then 7%. More importantly, the correlations are all greater than 0.99, indicating that the spatial and temporal variations in UTH (which are the focus of the this study) are very robust. Table 2 shows the results of restricting the training profiles to separate latitude belts: midlatitude summer (45°N-30°N), tropical (30°N-30°S), and midlatitude winter (30°S-45°S). Once again, the precise values of the coefficients differ, however the resulting UTH is insensitive to the regional or seasonal differences in training profiles.

Finally, as shown by Stephens et al. [1996] and others [Salathe and Smith, 1996; Soden and Lanzante, 1996], current uncertainties regarding the treatment of continuum absorption in existing transmittance models can lead to systematic biases in UTH of 10-15%. This uncertainty represents a limitation in our current theoretical understanding of continuum absorption and has important implications for the accuracy of all infrared-based water vapor retrievals. However, it is important to note that the spatial and temporal variability of UTH, which is the focus of the current study, is insensitive to the differences between various transmittance models [Stephens et al., 1996]. Thus while these absolute values of a particular UTH climatology may depend upon the transmittance model used in the retrieval, the spatial and temporal variations of UTH are very robust.

Since clouds strongly attenuate the emission of infrared radiation, estimation of the relative humidity requires information from pixels in which the $T_{6.7}$ is not affected by cloud cover. Given the vertical distribution of the 6.7 μm weighting function, this restriction usually corresponds to the exclusion of pixels containing middle and upper level clouds [Schmetz and Turpeinen, 1988]. Clear-sky $T_{6.7}$ are determined using a bispectral cloud-masking scheme described in SB93. This procedure estimates the cloud top temperature from the 11 μm channel and uses the difference in brightness temperatures between the 11 μm and the 6.7 μm channels ($\Delta T_b = T_{11} - T_{6.7}$) as a threshold to discriminate between clear and cloudy pixels. Pixels for which $\Delta T_b < 25$ K are considered to be cloud contaminated. This threshold is based on theoretical calculations of the effect of clouds on the 6.7 μm radiance (see section 4 of SB93) as well as on sensitivity calculations. It is important to note that the UTH distribution is not sensitive to reasonable

changes in this threshold. For example, changing the ΔT_b threshold from 25 K to 30 K results in rms differences in seasonal-mean UTH of < 1%. Additionally, any pixels that satisfy the ΔT_b threshold but have UTH values exceeding 100% are also assumed to be cloudy (typically < 2% of pixels). To provide a rough indication of the distribution of upper level cloud cover, Figure 2a shows the fraction of cloudy pixels. While this number is not intended to provide a rigorous estimate of the actual cloud amount, it does serve as a useful proxy for depicting regional variations in upper level cloudiness. The seasonal-mean fraction of cloudy pixels reflects well-known patterns of the cloud distribution and is in reasonable agreement with measurements of high cloud cover from the International Satellite Cloud Climatology Project (ISCCP) [cf. Hartmann et al., 1992; Figure 2]. For further details regarding the GOES 7 data characteristics and UTH retrieval the reader is referred to SB93.

2.2. Pattern Displacement Vectors

Trajectories of upper level water vapor are tracked by matching spatial features in successive water vapor images using time-lagged cross correlation. The procedure is, in principle, analogous to that used in satellite retrievals of "cloud motion" and "water vapor" winds [e.g. Laurent, 1993; Schmetz et al., 1995a; Velden et al., 1997]. The feasibility of this approach relies on the fact that over the short periods of time (e.g., 1 hour) the water vapor and clouds influencing the 6.7 μm radiance behave approximately as passive tracers drifting with the wind [Stewart et al., 1985]. Implicit in this approach is also the assumption that the features being tracked are associated with the advective motion of the atmosphere rather than propagating waves. Fortunately, for the scales of patterns being tracked here (< 500 km), the variations in temperature associated with propagating atmospheric disturbances such as gravity waves are typically < 1 K in the upper troposphere [Hamilton and Vincent, 1995; Allen and Vincent, 1995] and, consequently, have a much smaller effect on the $T_{6.7}$ relative to typical spatial variations in moisture or cloud cover [Soden and Bretherton, 1993]. Other propagating disturbances such as Kelvin or Rossby waves have much larger spatial scales compared to those being tracked here. Indeed, the trackability of water vapor features is largely dependent upon the degree of small-scale spatial contrast present in the

Table 2. Sensitivity of UTH Retrieval to Regional Variations in Training Profiles.

Region	a	b, K^{-1}	rms	Bias	Corr.
45°N-45°S	35.5	-0.130	0.0	0.0	1.0
45°N-30°N	36.8	-0.136	6.4	5.8	> 0.99
30°N-30°S	35.9	-0.132	3.8	3.4	> 0.99
30°S-45°S	38.2	-0.142	7.7	7.1	> 0.99

The values of the regression coefficients (a, b) obtained using July 1, 1987 ECMWF profiles from four different latitude regions are shown. To evaluate its sensitivity, the UTH was determined from one day of GOES $T_{6.7}$ observations using each set of coefficients. The rms difference (in %), bias (in %), and spatial correlation of each UTH estimate is then compared to that obtained from the full-domain coefficients (45°N-45°S).
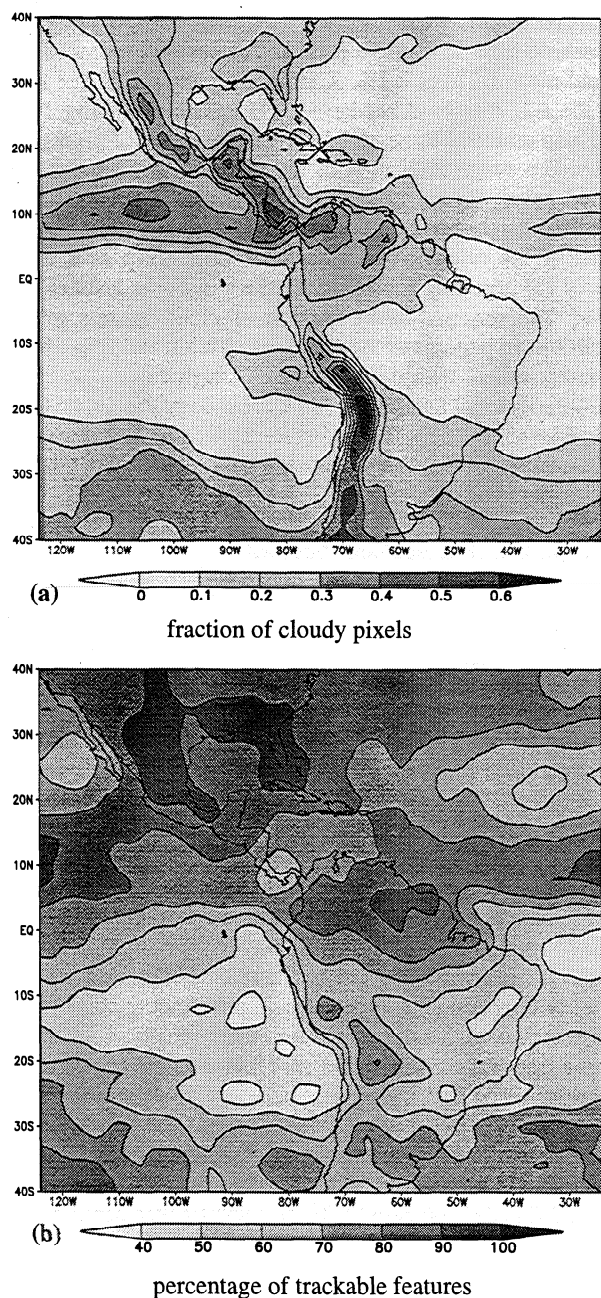
(a)

fraction of cloudy pixels

(b)

percentage of trackable features

Figure 2. (a) Fraction of cloudy pixels within each grid box time-averaged for June - August 1987. (b) The percentage of trackable 6.7 μm water vapor radiance patterns. The values represent the percentage of radiance patterns which satisfied both the forward and the backward pattern search criteria for JJA 1987. For clarity the field has been smoothed using a nine point spatial filter.

radiance field. Generally speaking, patterns consisting of cloud boundaries and large moisture contrasts are more easily tracked, while those consisting of cloud free regions with little moisture contrast are more difficult to track.

The tracking algorithm developed for this study starts by describing a reference "box" of ~(368 km)^2 at nadir on the initial image (Figure 3) which defines the origin and contains the spatial pattern of 6.7 μm radiances (in 8 km pixels) to be searched for on the ensuing image (1-hour later). While the GOES 7 6.7 μm imagery contains 8 km resolution data (at nadir), the actual footprint resolution of the sensor is 16 km. The

nominal 8km resolution imagery is created by oversampling each pixel element within a scan line. In the vertical, each scan line is repeated so that every other scan line is a duplicate of the preceding line. Consequently, the sampling interval between individual pixel data is 8 km (element) by 16 km (line). The tracking procedure accounts for this by removing every other line from the reference box. The resulting dimension of the reference box is then 46 pixels in the element direction by 23 pixels in the line direction. To facilitate the subsequent analysis, the initial reference boxes are predetermined and centered along an equally spaced 2° x 2° latitude/longitude grid. The spatial pattern of radiances contained in the reference box is compared with that in all boxes on the later image within a ~360 km radius, and the box containing the highest spatial correlation defines the destination box. A pattern displacement vector (PDV) is then determined from the centers of the reference and destination box.

Once the destination box is determined, the quality of the PDV is checked by performing a backward time-lagged cross correlation. The destination box now defines the pattern to be searched for, and the above procedure is repeated by searching backward in time for the highest spatial correlation in the earlier image. If the reverse pattern search returns to the original reference box, then the vector is considered reliable, otherwise the vector is discarded and no value is reported for that grid box. The philosophy behind the reverse pattern search is that the displacement vector should be independent of which image (i.e., which time) is used to define the reference box and that only reasonable matches will provide the same displacement for both directions. Any PDV for which the forward and backward displacements disagree by more than two line pixels or four element pixels are discarded. This corresponds to a maximum inconsistency between the forward and the backward PDVs of roughly ± 8 ms^{-1}. This rather generous threshold is used for accepting PDVs with the understanding that, for climatological studies such as this, random errors can be averaged out. Indeed, in a similar analysis, *Schmetz et al.* [1995b] also relaxed the quality control in their operational tracking algorithm for this reason. Finally, by assigning the PDV to the center of the reference box (rather than at some midpoint between the reference box and the destination box), it is assumed that the flow field is constant during the 1 hour tracking period. It is felt that the cost of introducing small noise into the data as a result of this assumption is outweighed by the advantage of having an equally distributed data set which greatly facilitates the analysis (such as the computation of time-average quantities). While this is sufficient when considering monthly mean products, such a procedure may be unsuitable for daily analysis.
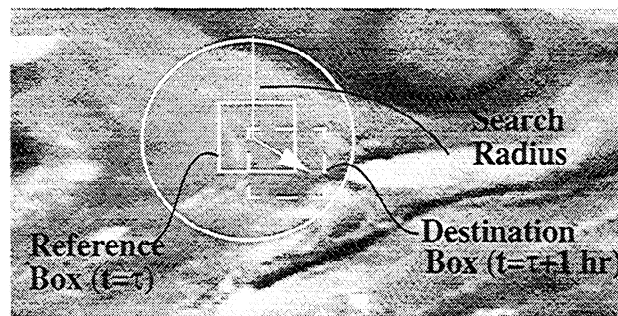

Figure 3. Schematic illustration of the pattern tracking algorithm.

Since the ability to trace features from one image to the next depends upon the nature of the radiance pattern being followed, the sampling of PDVs exhibits distinct regional variability. Figure 2b shows the percentage of water vapor radiance patterns which were successfully tracked (i.e., the percentage of patterns for which the forward and backward displacements converged) from once-daily imagery (0100-0200 UT) for the period of June-August 1987. This diagnostic provides a measure of the trackability of the water vapor radiance patterns. Note that the most easily tracked features (> 80%) correspond to regions of greatest cloudiness, whereas the most difficult patterns to track (< 50%) coincide with cloud free regions of the subtropics. This variation reflects the fact that the tracking algorithm is most successful in following features which contain large spatial contrasts in the radiance field and that clouds are a major contributor to these spatial contrasts. The convectively active regions also tend to exhibit larger spatial gradients in the upper tropospheric moisture compared to the subtropical regions, which further enhances their trackability.

To assess the quality of our tracking algorithm, the PDVs computed using the forward/backward pattern correlation method developed here is compared to water vapor wind vectors (WVWV) obtained from the CIMSS operational wind algorithm (Velden et al., 1997). The comparison is made by centering the reference box for our algorithm at the location of the WVWV and then performing the pattern search as described above. The WVWVs are determined using three images, 30 min apart, and include robust quality control checks (Velden et al., 1997). Our algorithm was applied to the first and last image (one-hour apart) and includes only the forward and backward consistency check. In this case the images used are from 1145, 1215, and 1245 GMT on June 4, 1995. The results are shown in Figure 4. Out of the 893 vectors obtained by the CIMSS algorithm, our algorithm was able to successfully track 732. Thus the forward and backward pattern search failed to converge on ~13% of the patterns for which the CIMSS algorithm successfully obtained vectors. However, it should be noted that during its quality control procedure the
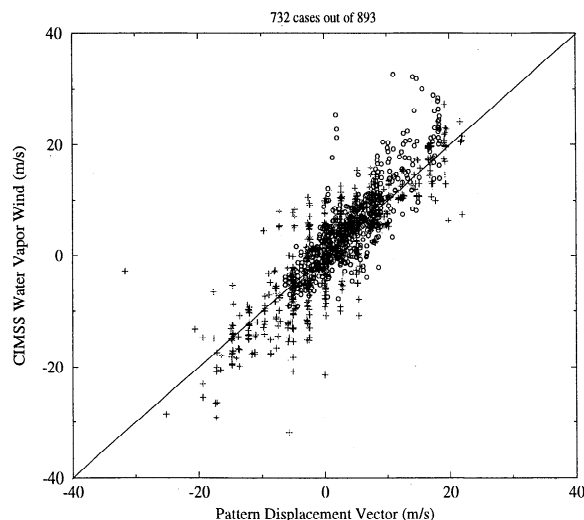

732 cases out of 893

Figure 4. Scatterplot comparing water vapor wind vectors (WVWV) from the algorithm of Velden et al. [1997] versus the corresponding PDVs computed using the algorithm described in section 2 for 1200 UT, June 4, 1995. Results are shown for both the u (circles) and the v (pluses) components.

CIMSS algorithm also discards a substantial number of winds which are not shown here. Hence this result is not intended to compare the relative sampling density of the two algorithms but simply to provide a measure of the consistency between the tracking component of the algorithms. Comparison of the WVWV with our PDV indicates that both vector components are well correlated ($r > 0.85$) with average absolute differences of < 4 m/s and biases of < 1m/s. Thus the pattern-tracking algorithm developed here compares favorably with displacements obtained using a more sophisticated tracking and quality control procedure.

The radiance patterns being tracked are generally confined to a narrow range of altitudes (~200-350 hPa) corresponding to the upper tropospheric layer flow [Schmetz et al., 1995b]. It is noted, however, that the height and thickness of the PDV varies depending upon the nature of the radiance pattern being tracked. Patterns containing significant cloud cover generally follow the motion of the cloud top, whereas pure water vapor patterns tend to track the outflow of deeper layers. Since assigning heights to the PDVs typically requires coincident model forecasts, no explicit height assignment is performed. Rather, the mean $T_{6.7}$ of the reference box is recorded to serve as a crude proxy of the PDV altitude. This provides a mechanism for characterizing variations in the altitude of the PDVs in terms of their temperature and can also be used for identifying vertical discontinuities in the PDV flow field. Generally speaking, PDVs located at higher altitudes exhibit colder brightness temperatures, while those at lower altitudes exhibit warmer brightness temperatures. For the range of viewing angles considered here, the effect of changes in satellite view angle upon the $T_{6.7}$ are typically smaller than the contrast between clear and cloudy patterns (which are the dominant source of altitude variation). Nevertheless, it is important to emphasize that this study focuses on interpreting the PDVs as a diagnostic measure of the upper tropospheric circulation, rather than on retrieving an explicit wind vector corresponding to a specified finite level of atmosphere. For this reason, the radiance pattern brightness temperature should only be interpreted as a crude proxy for the PDV altitude.

Figure 5 shows an example of the instantaneous PDV (arrows) and UTH (shaded) fields for 0100 UT on August 27, 1987. Grid boxes with no shading indicate regions where retrieval of UTH was not possible due to extensive upper level cloud cover. Several features are noteworthy. (1) The distribution of PDV exhibits spatially coherent circulations which closely coincide with moisture boundaries. This is particularly evident in the strong northwesterly flow over the southern Pacific ocean and southeastern Brazil, and in the anticyclonic circulation centered off the southeastern U.S. coast. (2) The PDVs tend to diverge surrounding regions of active tropical convection, as inferred from elevated UTH, over northern Brazil and Central America. (3) There are a greater number of missing PDVs over the subtropics where there is less spatial contrast in the radiances.

3. Upper Tropospheric Relative Humidity and the Large-Scale Atmospheric Circulation

This section presents results obtained from applying the UTH retrieval and pattern tracking algorithm to 3 months of data covering the period of June, July, and August (JJA) 1987. The PDVs are obtained for each day by tracking radiance pat-
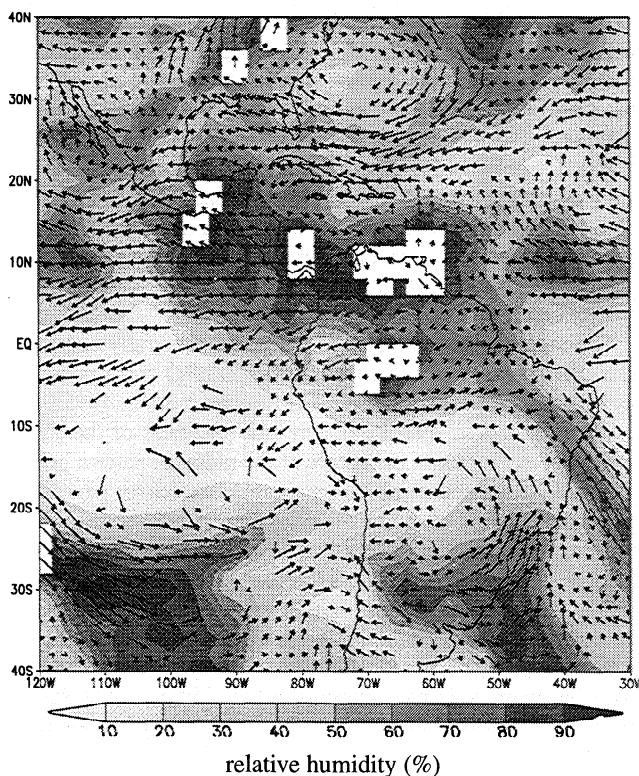
Figure 5. Upper tropospheric relative humidity (shaded) and pattern displacement vectors for 0100 UT, August 27, 1987.

terns 1 hour apart using images from 0100 and 0200 UT. If either the 0100 or 0200 imagery is missing, no PDV or UTH is reported for that day. The seasonal-mean UTH (shaded) and PDVs (arrows) shown in Figure 6a reveal clearly highlight the impact of the large-scale circulation on the distribution of upper tropospheric moisture. Humid regions (UTH > 60%) occur in a distinct band along the ITCZ and over the extratropical storm tracks, whereas dry regions (UTH < 20%) dominate the subtropics. The PDVs also exhibit coherent large-scale features consistent with the observed UTH distribution. Over regions of high UTH in the tropics, the PDVs indicate a diverging upper level flow, reflecting the upward movement of air by deep convection. Likewise, regions of low UTH in the subtropics are associated with converging PDVs, implying sinking air. The distribution and magnitude of the UTH is consistent with that described in previous studies [*Udelhofen and Hartmann*, 1995; *Velden et al.*, 1997]. The seasonal-mean brightness temperature of the patterns (Figure 6b) reveals distinct regional variations in the PDV altitude. Patterns over the tropical convective region and extratropical storm tracks exhibit colder temperatures (higher altitudes) due to the abundance of upper level clouds in these regions. In contrast, the PDVs over the subtropical oceans exhibit warmer temperatures (lower altitudes) due to the lack of cloud cover and relative dryness of the upper troposphere.

The similarities between the upper tropospheric relative humidity and the time-mean circulation are more easily seen by examining the divergence of the seasonal-mean PDVs (Figure 7). An elongated band of upper level divergence is clearly evident along the ITCZ in close proximity to the band of high UTH. Regional structures in both the UTH and the divergence fields also exhibit a distinct geographic dependence, particularly over large islands and peninsulas of the Caribbean. For example, the Central American isthmus, Mexican plateau,

greater Antilles, and Florida peninsula are all easily distinguished in both the UTH and the divergence fields. Likewise, regions of low UTH over the subtropics coincide with regions of upper level convergence. If one assumes that the upper lev-
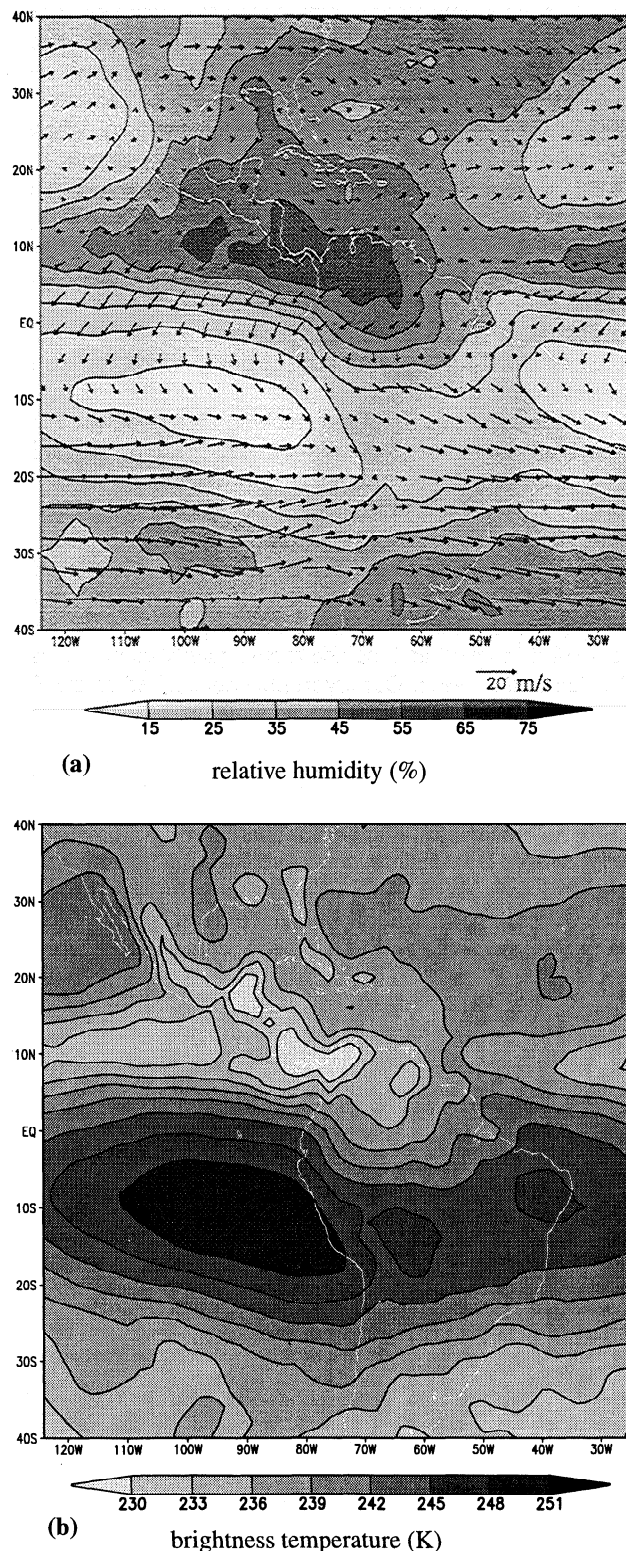

(a) relative humidity (%)

(b) brightness temperature (K)

Figure 6. (a) Seasonal-mean upper tropospheric relative humidity (shaded) and displacement vectors for June - August 1987. For clarity, only every other vector is shown. (b) The seasonal-mean brightness temperature of the 6.7 μm radiance patterns for June - August 1987.
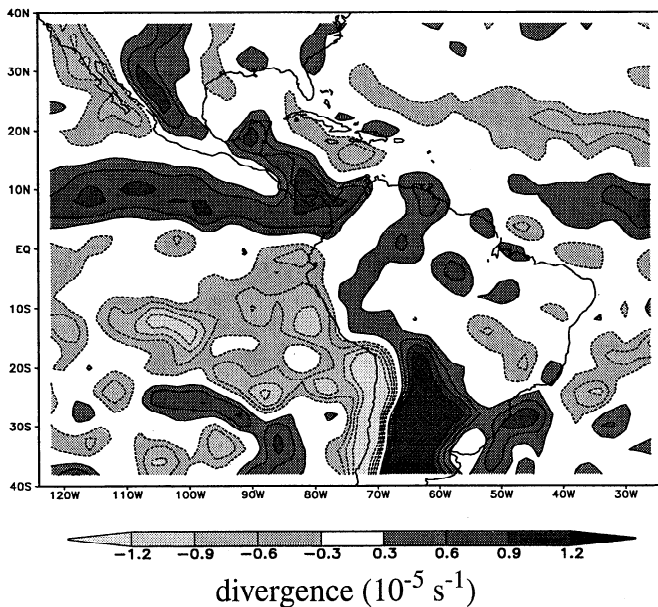
Figure 7. Divergence (10^{-5} s^{-1}) of the seasonal-mean pattern displacement vectors for June - August 1987. For clarity, the field has been smoothed using a nine point spatial filter.

el convergence observed for the subtropics (2×10^{-6} - 4×10^{-6} s^{-1}) takes place over a layer ~150 hPa thick [*Schmetz et al*, 1995b], the implied subsidence rate is ~20 - 50 hPa d^{-1}, which is typical for subtropical trade regions [*Sherwood*, 1996a; *Betts and Ridgeway*, 1989]. However, the conspicuously large divergence/convergence rates along Chile is believed to be an artifact of the Andes mountain range influencing the 6.7 micron radiance patterns.

The close relationship between the UTH and the divergence is also evident in the zonal mean of these fields (Figure 8a). To highlight the altitude dependence of the divergence field, the PDVs have been binned into cold patterns ($T_{6.7} < 240$ K) and warm patterns ($T_{6.7} > 240$ K) and the divergence computed separately for both (Figure 8b). As expected, the colder (higher altitude) patterns exhibit a stronger divergence over the tropics relative to the warmer (lower altitude) patterns, consistent with the observation that the atmospheric divergence tends to increase with height within the upper layer of the troposphere. The similarity between UTH and the PDVs divergence clearly highlights the dependence of upper tropospheric relative humidity upon the vertical motion of the atmosphere over a range of spatial scales. Indeed, this observation is consistent with previous satellite-based studies of the relationship between UTH and atmospheric circulation [e.g., *Picon and Desbois*, 1990; *Schmetz et al.*, 1995a, b; *Velden et al.*, 1997].

4. Lagrangian Tendencies of UTH

The previous section focused on examining the spatial distribution of water vapor pattern displacements and their similarity to the derived upper tropospheric humidity field. In addition to the Eulerian view, the high space/time resolution of the GOES imagery also provides the capability of monitoring upper tropospheric water vapor from a Lagrangian perspective. In this section, we examine the time rate-of-change of UTH within a given water vapor pattern as it is tracked from one image to the next. This analysis provides a unique perspective on the processes governing the moisture distribu-

tion that has not previously been measured from satellite observations. Recently, Salathe and Hartmann (1997) performed a trajectory analysis of the upper tropospheric moisture using analyzed wind fields and radiatively driven cooling to construct upper tropospheric moisture trajectories. While their technique for computing the trajectories is quite different from the pattern-tracking approach used here, it will be shown that both studies share many similar conclusions.

When analyzing the growth and decay of relative humidity experienced by a water vapor pattern, it is useful to consider fractional change in UTH given by $d\ln UTH/dt$. In this study, the fractional change in UTH is computed for each water vapor pattern by differencing the UTH between the reference box at 0100 UT and destination box 1 hour later (see Figure 3). This difference provides a measure of the change in UTH experienced by the layer as it moves horizontally along a trajectory. If the UTH is not obtainable from the pattern at either time, then the difference is flagged as missing. Note that the pattern tracking is entirely two-dimensional; consequently, no account is made for the vertical advection of air out of the UTH layer. Hence the trajectory is not a true three-dimensional Lagrangian depiction of the moisture transport, but rather represents the horizontal movement of a layer of upper tropospheric moisture. Given typical subsidence rates of ~30 hPa d^{-1} (~1 hPa h^{-1}) relative to the depth of the UTH layer (~300 hPa), attention will be focused on the tendency over short periods of time where the amount of air advected vertically out of the UTH layer is small compared to the depth of the layer itself.

Using the imagery for 0100 and 0200 UT, UTH tendencies are computed once per day and averaged over the period of JJA 1987. The seasonal mean tendencies are then zonally-av-
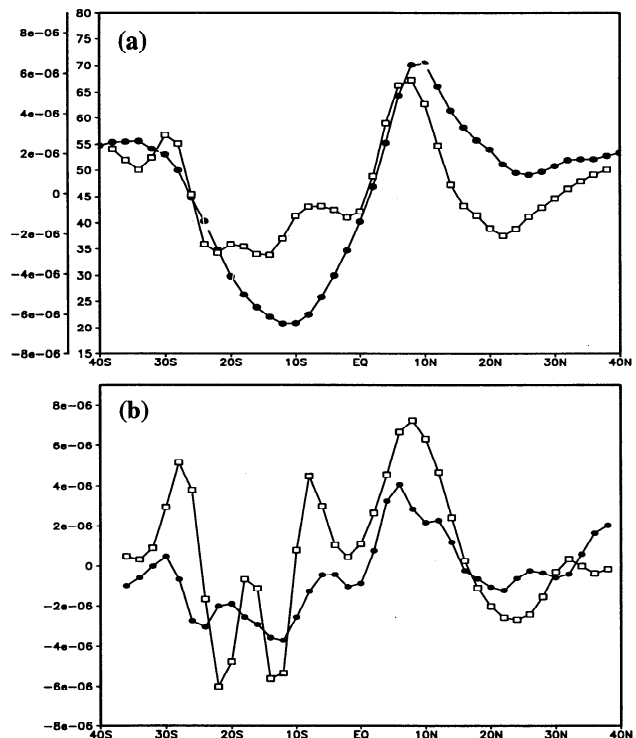

Figure 8. (a) Zonal-mean UTH in % (circles) and divergence of the PDVs (s^{-1}) for all patterns (squares). (b) The zonal-mean divergence (s^{-1}) of the PDVs for patterns with $T_{6.7} > 240$ K (circles), patterns with $T_{6.7} < 240$ K (squares).
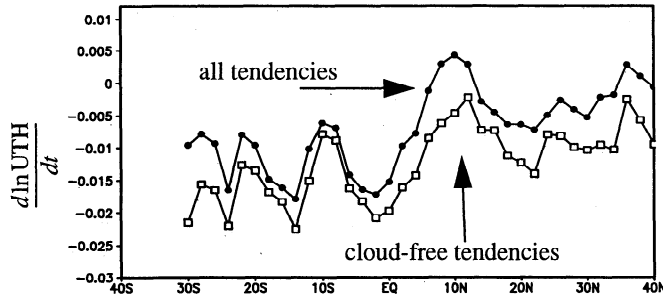
Figure 9. One hour humidity tendencies. The fractional change in upper tropospheric humidity ($d\ln UTH/dt$) computed from 1 hour displacements of water vapor trajectories (in units of hr^{-1}). The tendencies are time averaged for June - August 1987 and then zonally averaged for the GOES viewing domain ($125°W$ to $25°W$). The circles represent tendencies computed from all available UTH data. The squares represent tendencies computed from only UTH data for which fewer than 5% of the pixels in the grid box were cloudy.

eraged over the GOES viewing domain ($125°W-25°W$) to highlight the latitudinal structures (circles in Figure 9). The chief feature of this plot is that the tendencies are overwhelmingly negative. This indicates that when viewed from a Lagrangian perspective the upper troposphere becomes increasingly drier with time. While perhaps seeming unrealistic, this feature is entirely consistent with the sampling of the UTH data. Because UTH is only retrieved from cloud-free pixels, the UTH tendencies represent the change in moisture occurring within the clear-sky portion of the pattern. Since clear-sky regions are dominated by large-scale subsidence, the air in these regions becomes warmed via compressional heating and, in the absence of moisture sources, the relative humidity decreases. Consequently, one would expect to observe a systematic drying of the clear-sky upper troposphere, and the results of Figure 9 are consistent with this picture. This result is also consistent with the analysis of *Salathe and Hartmann* [1997] who noted a decrease in UTH along clear-sky trajectories based upon computations from analyzed wind fields (see their Figure 8). This consistency is reassuring, given the markedly different methods used for calculating the trajectories and UTH tendencies.

To further assist in the interpretation of the UTH tendencies, consider an idealized atmosphere in which the relative humidity, $r = q/q_s$, is independent of height over the range of upper tropospheric levels of concern, thus $d\ln r/dt = d\ln UTH/dt$. In the absence of moisture sources or sinks (e.g., evaporation, condensation, or subgrid mixing), the water vapor mixing ratio q remains constant, and the fractional change in relative humidity is equal to the negative fractional change in saturation mixing ratio q_s,

$$\frac{d}{dt}\ln UTH = \frac{d}{dt}\ln\frac{q}{q_s}$$

$$= -\frac{d}{dt}\ln q_s \qquad (2)$$

Thus a decrease in UTH represents an increase in the saturation vapor pressure within the UTH layer. Since q_s scales exponentially with temperature, doubling approximately every 10 K for the upper troposphere, to a close approximation, $d \ln q_s \approx 0.1 \; dT$. Accordingly, the change in UTH can be related to the change in temperature of the layer

$$\frac{d}{dt}\ln UTH \approx -0.1\frac{dT}{dt} \qquad (3)$$

This expression indicates that in the absence of moisture sources and sinks over the 1 hour tracking period the fractional change in UTH corresponds roughly to the change in temperature of the UTH layer scaled by a factor of -0.1. Under these conditions, the subtropical drying rates presented in Figure 9 imply a warming of roughly 1.5 to 2 K d^{-1}. In a Lagrangian framework, the temperature tendency reflects the combination of both adiabatic (e.g., compressional heating associated with isentropic subsidence) and diabatic (e.g., radiative cooling) processes as dictated by the thermodynamic energy equation

$$\frac{dT}{dt} = \frac{kT\omega}{p} + \frac{\dot{H}}{c_p} \qquad (4)$$

Considering a representative level in the tropical upper troposphere ($T=240$ K, $p=350$ hPa) experiencing a typical clear-sky radiative cooling rate of $\dot{H}/c_p \approx -1.5$ K d^{-1} [*Salathe and Hartmann*, 1997], the subsidence necessary to explain the observed drying rates range from ~15-20 hPa d^{-1} which is in reasonable agreement with subsidence rates noted for clear-sky regions of the tropics [*Sherwood*, 1996b]. Thus both the sign and the magnitude of the UTH tendencies are consistent with the impact of large-scale subsidence in drying the clear-sky upper troposphere.

An interesting aspect of the UTH tendencies is that the rate of upper tropospheric drying is not uniform but varies systematically with latitude, suggesting that air over the dry subtropical trade regions ($10°-30°S$) tends to dry out proportionally faster than air over the more humid regions of the tropics ($5°-15°N$) and extratropics ($> 35°N$). The slower drying rates observed in the tropics could result from the presence of moisture sources, such as the evaporation of hydrometeors from adjacent clouds. Indeed, such a mechanism has been found to be critical in regulating the upper tropospheric moisture in simple models of tropical convection [e.g., *Sun and Lindzen*, 1993; *Renno et al.*, 1994]. To examine whether grid boxes associated with greater cloudiness exhibit systematic differences in drying rates, the humidity tendencies for each day were screened according to the number of cloudy pixels and averages were computed from patterns containing little or no clouds (< 5% cloudy pixels). The results are labeled cloud-free UTH tendencies (squares) in Figure 9. For all latitudes, the UTH tendencies averaged from all grid boxes (circles) dry out more slowly than the tendencies averaged from the cloud-free grid boxes. The differences are most obvious in areas where upper level cloud cover is largest, such as along the tropics and northern subtropics where drying rates differ by up to a factor of 2. While these results cannot confirm that evaporation of hydrometeors is actually responsible for the difference, the larger drying rates observed for cloud-free regions is qualitatively consistent with this mechanism.

5. Water Vapor Pattern Trajectories

In this section, trajectories of upper tropospheric water vapor are constructed by sequentially tracking radiance patterns from consecutive images covering a 48 hour period. These water vapor pattern trajectories are derived by applying the tracking algorithm in a serial fashion. Starting from an initial target box at time $t=\tau$, the tracking algorithm searches for the

highest spatial correlation between this pattern and all possible destinations 1 hour later (t=τ + 1 h) $r_{\tau,\tau+1}$. If this pattern is successful tracked, the destination box at time t=1 now becomes the new target box and the algorithm searches for the highest spatial correlation between this pattern and all possible destinations at time (t=τ + 2 hr) $r_{\tau+1,\tau+2}$. A water vapor pattern trajectory is then constructed by repeating this procedure sequentially throughout a 48 hour period (beginning at 0000 UT of each day). To facilitate the pattern tracking, the target box has been expanded to a dimension of 60 pixels by 30 pixels. Hence the algorithm tracks a slightly larger scale of flow than discussed in the previous sections. Because of the inherent difficulty of objectively tracking water vapor patterns, it is rare for the tracking algorithm to successfully track 48 consecutive water vapor patterns. For instances where the forward and backward pattern searches are in disagreement, the trajectory is interpolated using the PDV from the previous search (1 hour prior). The subsequent analysis is then restricted to those pattern trajectories which contain fewer than 10% interpolated values.

Two trajectory analyses are performed. First, moisture features emanating from convective regions are tracked to characterize the destination and evolution of water vapor patterns leaving convective towers. Then, by reversing the temporal sequencing and tracking features backward in time, we examine where water vapor patterns entering the subtropical subsidence regions originate and how the humidity field changes along these trajectories. An ensemble of trajectories is calculated for two domains, a tropical convective domain which extends from 5°N-15°N and 110°W-60°W, and a subtropical subsidence domain which extends from 5°S-20°S, 110°W-60°W. The boundaries of these domains are chosen to encompass regions of active convection and subsidence over both land and ocean. The subtropical domain is slightly larger than the tropical domain owing to the greater difficulty of tracking subtropical water vapor patterns. Within each domain, trajectories are computed for each day starting at 00 GMT and lasting up to 48 hours. The origins of the trajectories (i.e., the initial target boxes) are equally distributed throughout the domain, separated by 5° latitude and 10° longitude. This procedure is performed for all days within the month of August 1987. After the quality of the trajectories is screened for interpolated values (see above), each domain typically has ~250 trajectories remaining which are analyzed below.

5.1. Tropical Forward Trajectories

First we consider where the moisture patterns exiting convective regions go. Figure 10 (top) illustrates the geographical displacement of the water vapor pattern trajectories for the tropical domain. The chief feature here is the distinct divergence of patterns away from the convectively active regions along the Central American isthmus. The westward propagation of the pattern trajectories reflects the passage of convective disturbances (e.g., easterly waves) along the ITCZ. Near the southern edge of the domain, most of the patterns track in a southward direction highlighting the upper level transport of moisture from the ITCZ into the subtropical subsidence zones. Northward propagating patterns are also observed, although they are fewer in number and tend to be concentrated along the northern edge of the convective zone. Typical displacements for the tropical trajectories are ~1000-1500 km over the 48 hour period.

A composite plot of the forward trajectories is presented in Plate 1 (top) as a function of the relative change in latitude and longitude. This diagram shows the location of the destination box for each trajectory at 12 hourly intervals: 12 hours (blue), 24 hours (green), 36 hours (yellow), and 48 hours (red). The relative displacements of the trajectories with respect to their original starting location were computed and then superimposed on top of each other. In general, the meridional displacements tend to be smaller than the zonal displacements, with few patterns tracking more then 10° latitude or 15° longitude over the 48 hours. The vast majority of the patterns propagate into the southwestern quadrant (~75%), highlighting the northerly and easterly flow which dominates this region. Of the northward moving trajectories the majority also tend to track westward although those in the northeastern quadrant tend to penetrate farther merdionally.

5.2. Subtropical Backward Trajectories

Next, the origin for water vapor patterns entering the subsidence region is examined. Figure 10 (bottom) shows the 48 hour backward trajectories computed for patterns which arrived in the subtropical domain (110°W-60°W, 5°S-20°S).
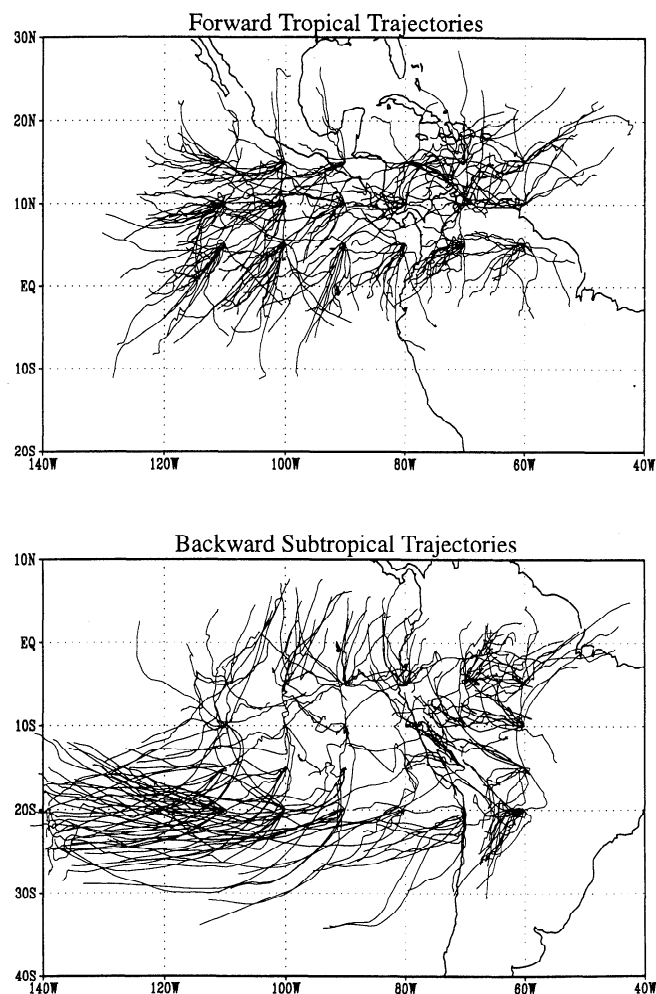

Figure 10. Water vapor radiance pattern trajectories computed from forward pattern displacements originating in the tropical region (top) and from backward pattern displacements arriving in the subtropical region (bottom). Trajectories are computed over a 48 hour period.
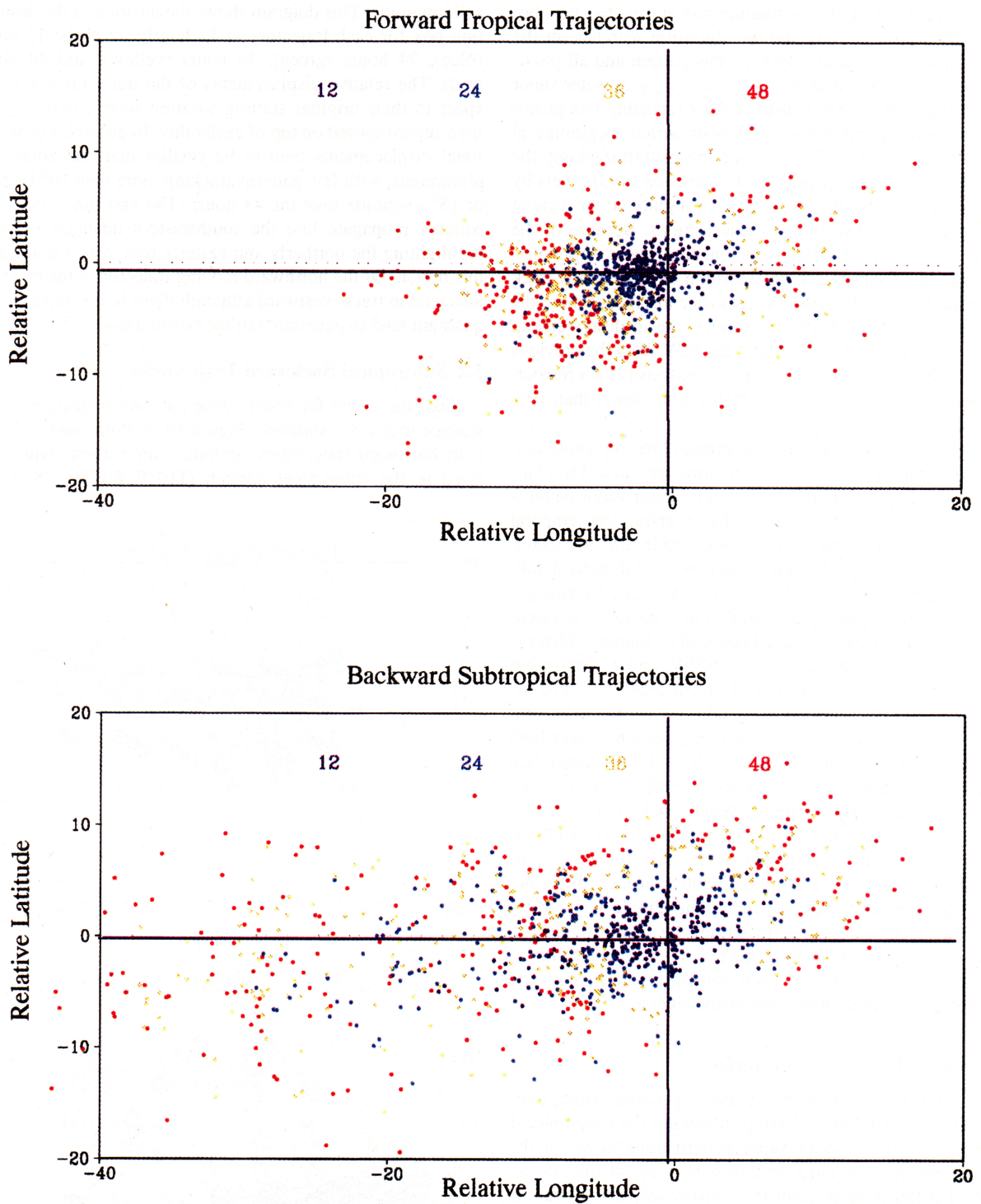
Plate 1. Scatterplot depicting the pattern location after 12 hours (blue), 24 hours (green), 36 hours (yellow), and 48 hours (red). Results are shown for forward trajectories leaving the tropical domain (top) and for backward trajectories entering the subtropical domain (bottom).

This plot reveals two distinct pathways for moisture patterns entering the subtropical dry zone: an ITCZ path and an SPCZ path. For moisture patterns entering the northern edge of the subtropics (5-10°S) the primary origin tends to be southwestward propagating disturbances from the ITCZ. This is consistent with the forward trajectories (Plate 1, top) which also shows water vapor patterns traveling southward from the ITCZ into the northern edge of the subtropics. However, for moisture patterns entering the southern portion of the subtropics (15°S-20°S), the primary source appears to be moisture transported zonally from eastward propagating disturbances along the SPCZ. These trajectories are characterized by much larger zonal displacements relative to the meridional displacement, and an obvious eastward propagation as opposed to the slight westward propagation noted for the ITCZ-originating disturbances. The SPCZ trajectories result from low-latitude disturbances that propagate southeastward as they interact with transient troughs in the midlatitude westerlies [e.g., *Kiladis et al.*, 1989; *Vincent*, 1994]. This interaction with the mid-latitude westerlies results in the much larger zonal displacements noted for these trajectories. An example of an SPCZ-originating disturbance is evident in the bottom left-hand corner of Figure 5. Note, however, that few patterns enter the subtropics from regions poleward of 30° latitude, consistent with the conclusions of *Sherwood* [1996b]. The contrast between the ITCZ and the SPCZ paths is also evident in the composite plot of the backward trajectories (Plate 1, bottom). The backward trajectory composites show two clusters, one for trajectories that track primarily southward while also moving either eastward or westward (the ITCZ path) and the others that track primarily eastward (up to 40° longitude) while also moving either northward or southward (the SPCZ path).

Average trajectories (Figure 11), plotted in terms of the relative change in latitude and longitude with respect to the original starting location, more clearly highlight the difference between the two pathways. Averages are computed from all trajectories within the subtropical domain (solid line), trajec-
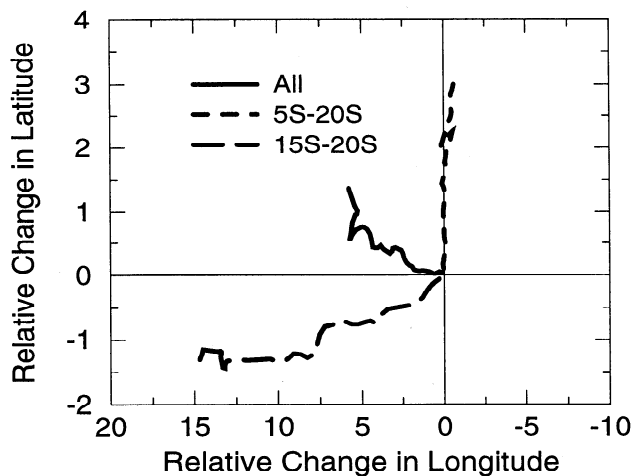

Figure 12. Lagrangian evolution of UTH and radiance pattern correlations. The upper tropospheric relative humidity (left) and time-lagged cross correlation of the radiance patterns (right) shown as a function of time for forward trajectories originating in the tropical convective domain (top) and for backward trajectories arriving in the subtropical subsidence domain (bottom).

tories entering the northern half of the domain 5°S-10°S (dotted line), and trajectories entering the southern half of the domain 15°S-20°S (dashed line). The mean pathway is clearly composed of trajectories with two very different characteristics. Water vapor patterns arriving into the northern half of the subtropical domain exhibit a relatively large southward displacement with little systematic zonal displacement. On the other hand, patterns arriving into the southern half of the subtropical domain exhibit very large eastward displacements combined with a small northward displacement. Thus moisture patterns entering the dry subtropical region are not strictly associated with convective outflow from the ITCZ. Rather, the SPCZ also provides an important source of moisture. This feature was also noted by Salathe and Hartmann (see their Figure 5a). Since the origin and maintenance of the SPCZ involves a hybrid interaction between low-latitude convective disturbances and higher latitude transient waves (Vincent, 1994), this evidence suggests that a complete picture of the processes regulating the driest and most radiatively transparent regions of the subtropics may require consideration of both types of disturbances. It should also be emphasized that the current analysis is limited to a single season (JJA) from one year (1987). Further analysis is necessary to understand the importance of seasonal and interannual changes in the tropical circulation for this region.

Figure 11. Average back trajectories computed from all trajectories originating within the subtropical domain 5 S-20 S (solid line), trajectories originating from the northern half of the domain 5°S-10°S (dotted line), and trajectories originating from the southern half of the domain 15°S-20°S (dashed line). Results are plotted in terms of the relative change in latitude and longitude with respect to the original starting location.
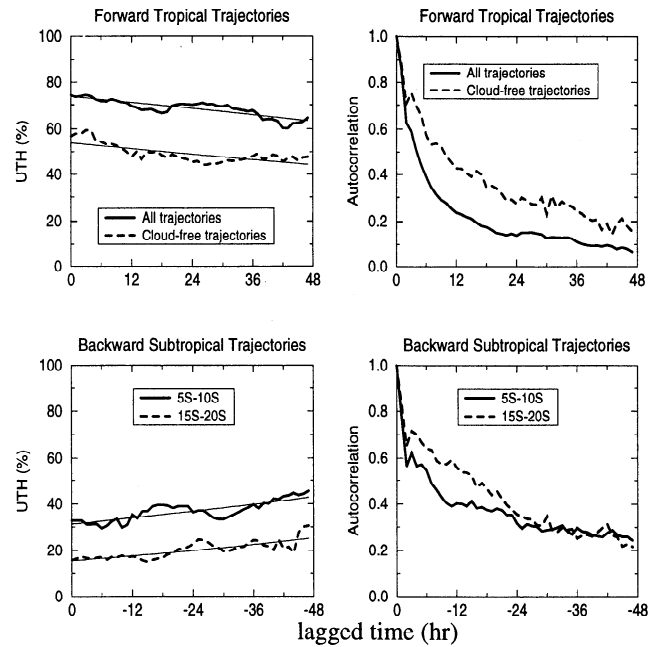
5.3. Trajectory Evolution of UTH and Radiance Patterns

In this section, the evolution of the moisture content along the convective and subsidence trajectory paths is considered. Figure 12 (left) shows the average UTH of the destination box as a function of increasing time for forward trajectories emanating from the tropical domain (top) and as a function of de-

creasing time for backward trajectories arriving at the subtropical domain (bottom). For the tropical trajectories the UTH decreases with increasing age as the air is expelled away from the convective region, subsides, and dries. On average, the UTH (solid line) decreases from ~75% at the initial time to slightly over 60% forty-eight hours later. Averages were also computed from cloud-free trajectories (dashed line). The fractional drying tendency for the entire 48 hour period was also computed through a linear regression of ln(UTH) versus time (shown as straight lines in Figure 13). In addition to being systematically drier, the "cloud-free" trajectories also tend to dry out slightly faster ($d\ln UTH/dt$ = -0.06 hour^{-1}) than the average of all trajectories ($d\ln UTH/dt$ = -0.03 hour^{-1}).

Note that the patterns dry out more slowly between 24 and 48 hours than during the first 24 hours. This likely reflects the impact of subgrid processes in altering the humidity content of the pattern by mixing with surrounding air. This is supported by the time-lagged autocorrelation of the radiance patterns (Figure 12, right) which shows that the autocorrelation drops off significantly during the first day of tracking with e-folding times of ~9 hours for all trajectories and ~18 hours for cloud free trajectories. The shorter decorrelation times for cloudy patterns reflect the more transient nature of cloud cover relative to pure (cloud-free) water vapor features. Thus, after relatively short periods of time (< 1 day) the pattern being tracked bears little resemblance to the pattern which was initially targeted, presumably due to the role of sub-grid mixing in shearing and distorting the original pattern. This suggests that for time periods longer than 1 day, the concept of a Lagrangian trajectory at these spatial scales has little meaning. That is, that the role of sub-grid processes begins to dominate over the effects of large-scale advection.

For the backward trajectory calculations (Figure 12, bottom) the evolution of the UTH field is shown separately for the ITCZ-originating patterns (5°-10°S) and SPCZ-originating patterns (15°-20°S). For both pathways, patterns entering the subtropical region become increasingly moist as one follows them back in time. During the first 24 hours, both sets of trajectories moisten fairly steadily. After this period the trajectories from the SPCZ path appear to moisten more slowly, perhaps due to sub-grid entrainment of drier air. Compared to the tropical patterns, water vapor patterns over the subtropical regions tend to dry out slightly faster on average ($d\ln UTH/dt$ = −0.009 hr^{-1}), consistent with the results of section 4. Also note that the decorrelation times of the subtropical radiance patterns (Figure 12, right) are noticeably longer than those in the tropics, reflecting a systematically slower dispersion of the water vapor patterns in the subtropics relative to the tropics.

6. Conclusions

Geostationary satellite observations of hourly water vapor radiances are used in conjunction with an objective pattern-tracking algorithm to follow water vapor features from sequential time-lapsed imagery. The primary accomplishments of this investigation are summarized as follows:

1. The spatial patterns of upper tropospheric moisture closely reflect patterns in the upper level circulation, with regions of high (low) relative humidity coinciding with regions of upper level divergence (convergence). This close correlation between humidity and divergence, even on regional scales, clearly emphasizes the importance of the time-mean circulation in regulating the distribution and variation of up-

per tropospheric moisture and is consistent with several previous studies. It also suggests that to a first approximation global measurements of UTH from polar orbiting satellites can provide valuable information for characterizing seasonal-to-interannual variations in the tropical circulation.

2. By examining the trend in UTH as moisture patterns are tracked from one image to the next, information on the Lagrangian behavior of the UTH field is obtained. On average, the clear-sky UTH is observed to decrease with time reflecting the role of large-scale subsidence in drying the upper troposphere. When categorized according to cloud amount, the analysis reveals that water vapor patterns associated with little or no clouds dry out substantially faster than those with clouds. This suggests that the evaporation of cloud condensate may be an important factor in regulating the drying rate of the upper troposphere, although its impact is generally restricted to regions of extensive cloud cover.

3. Trajectories of upper tropospheric water vapor were also constructed by sequentially tracking radiance patterns from consecutive images spanning a 48 hour period. For JJA 1987, this analysis reveals two distinct paths for water vapor entering the dry subsidence region of the subtropical South Pacific. One path highlights the southward propagation of convective outflow from the ITCZ while the other path reflects the injection of moisture from eastward propagating disturbances along the SPCZ. Thus understanding moisture variations in this region will likely require consideration of both types of convective systems.

4. The trajectory analysis also indicates that for the spatial scales considered here (~400 km), the Lagrangian timescales of upper tropospheric water vapor radiance patterns are of the order of 1 day or less. At longer timescales, subgrid processes appear to have a more dominant effect on the humidity patterns than large-scale advection and the concept of a Lagrangian trajectory (at these spatial scales) becomes unclear. This may place important limitations on the reconstruction of Lagrangian trajectories from analyzed wind fields.

While the present study has focused on observations from a single satellite, there are currently four geostationary satellites in operation which provide full-disk coverage of upper tropospheric water vapor radiances. Such data offer the opportunity to perform a near-global analysis of the upper tropospheric moisture and circulation for characterizing the moisture sources of dry subtropical regions in other parts of the globe. Additionally, current GOES archives contain hourly water vapor imagery dating back to the mid-1980s, which should provide valuable insight into the seasonal-to-interannual variability of the upper tropospheric moisture and circulation fields over the American sector of the globe. Future efforts will be directed toward such studies.

References

Allen, S. J., and R. A. Vincent: Gravity wave activity in the lower atmosphere: Seasonal and latitudinal variations, *J. Geophys. Res.*, 100, 1327-1350, 1995.

Bates, J. J., X. Wu, and D. L. Jackson: Interannual variability in upper tropospheric water vapor band brightness temperature, *J. Clim.*, 9, 427-438, 1996.

Betts, A. and W. Ridgway: Climatic equilibrium of the convective boundary layer over the tropical ocean, *J. Atmos. Sci.*, 46, 2621-2641, 1989.

Eyre, J. R.: A fast radiative transfer scheme for satellite sounding systems, *ECMWF Tech. Memo. 176*, Eur. Cent. for Medium-Range Weather Forecasting, Reading, England, 1991.

Hamilton, K. and R. A. Vincent: High-resolution radiosonde data offer new prospects for research, *EOS Trans. AGU*, 76, 497-507, 1995.

Hartmann, D. L., M. E. Ockert-Bell, and M. L. Michelsen: The effect of cloud type on Earth's energy balance: Global analysis, *J. Clim.*, 5, 1281-1304, 1992.

Jedlovec, G.J., R.J. Atkinson, and J.A. Lerner: Upper-level water vapor transport from GOES data. paper presented at the 13th Conference on Hydrology, Am. Meteor. Soc., Long Beach, Calif., 1997.

Kiladis, G. N., H. von Storch, and H. van Loon: Origin of the South Pacific Convergence Zone, *J. Clim.*, 2, 1185-1195, 1989.

Laurent, H.: Wind extraction from Meteosat water vapor channel image data, *J. Appl. Meteorol.*, 32, 1124-1133, 1993.

Picon, L., and M. Desbois: Relation between METEOSAT water vapor radiance fields and large-scale tropical circulation features, *J. Clim.*, 3, 865-876, 1990.

Pierrehumbert, R. T.: Thermostats, radiator fins and the local runaway greenhouse effect, *J. Atmos. Sci.*, 52, 1784-1806, 1995.

Renno, N. O., K. A. Emanuel, and P. H. Stone: Radiative convective model with an explicit hydrologic cycle 1. Formulation and sensitivity to model parameters, *J. Geophys. Res.*, 99, 14,429-14,441, 1994.

Salathe, E. P., and D. L. Hartmann, A trajectory analysis of tropical upper-tropospheric moisture and convection, *J. Climate*, 10, 2533-2547, 1997.

Salathe, E. P. and R. B. Smith: Comparison of 6.7 μm radiance computed from aircraft soundings and observed from GOES, *J. Geophys. Res.*, 101, 21,303-21,310, 1996.

Schmetz, J. and O. M. Turpeinen, Estimation of the upper tropospheric relative humidity field from METEOSAT water vapor image data, J. *Clim. Appl. Meteorol.*, 27, 889-899, 1988.

Schmetz, J., W. P. Menzel, C. Velden, X. Wu, L. van de Berg, S. Nieman, C. Hayden, K. Holmund, and C. Geijo: Monthly mean large-scale analyses of upper tropospheric humidity and wind fields derived from three geostationary satellites, *Bull. Am. Meteorol. Soc.*, 76, 1578-1584, 1995a.

Schmetz, J., C. Geijo, W. P. Menzel, K. Strabala, L. van de Berg, K. Holmund, and S. Tjemkes: Satellite observations of upper tropospheric relative humidity, clouds and wind field divergence, *Beitr. Phys. Atmos.*, 68, 345-357, 1995b.

Sherwood, S. C.: Maintenance of the free-tropospheric tropical water vapor budget distribution. Part I: Clear regime budget, *J. Clim.*, 9, 2903-2918, 1996a.

Sherwood, S. C.: Maintenance of the free-tropospheric tropical water vapor budget distribution. Part II: Simulation by large-scale advection, *J. Clim.*, 9, 2919-2934, 1996b.

Soden, B. J.: Variations in the tropical greenhouse effect during El Nino, *J. Clim.*, 10, 1050-1055, 1997.

Soden, B. J. and F. P. Bretherton: Upper tropospheric relative humidity from the GOES 6.7 μm channel: Method and climatology for July 1987, *J. Geophys. Res.*, 98, 16,669-16,688, 1993.

Soden, B. J., and R. Fu: A satellite analysis of deep convection, upper tropospheric humidity and the greenhouse effect, *J. Clim.*, 8, 2333-2351, 1995.

Soden, B. J. and F. P. Bretherton: Interpretation of TOVS water vapor radiances in terms of layer-average relative humidities: Method and climatology for the upper, middle and lower troposphere, *J. Geophys. Res.*, 101, 9333-9343, 1996.

Soden, B. J., and J. R. Lanzante: An assessment of satellite and radiosonde climatologies of upper tropospheric water vapor, *J. Clim.*, 9, 1235-1250, 1996.

Spencer, R. W., and W. D. Braswell: How dry is the tropical free troposphere? Implications for global warming theory, *Bull. Am. Meteorol. Soc.*, 78, 1097-1106. 1997.

Stephens, G. L., D. A. Randall, I. L. Wittmeyer, D. A. Dazlich, and S. Tjemkes: The earth's radiation budget and its relation to atmospheric hydrology 3. Comparison of observations over oceans with a GCM, *J. Geophys. Res.*, 99, 4391-4950, 1993.

Stephens, G. L., D. L. Jackson, and I. Wittmeyer: Global observations of upper-tropospheric water vapor derived from TOVS radiance data, *J. Clim.*, 9, 305-326, 1996.

Stewart, T. R., C. M. Hayden, and W. L. Smith: A note on water vapor wind tracking using VAS data on McIDAS, *Bull. Am. Meteorol. Soc.*, 66, 1111-1115, 1985.

Sun, D.Z., and I.M. Held: A comparison of modeled and observed relationships between interannual variations of water vapor and temperature, *J. Clim.*, 9, 665-675, 1996.

Sun, D. Z., and R. S. Lindzen, 1993: Distribution of tropical tropospheric water vapor, *J. Atmos. Sci.*, 50, 1644-1660.

Thompson, S. L., and S. G. Warren: Parameterization of outgoing infrared radiation derived from detailed radiative calculations, *J. Atmos. Sci.*, 39, 2667-2880, 1982.

Udelhofen, P. M. and D. L. Hartmann: Influence of tropical cloud systems on the relative humidity in the upper troposphere, *J. Geophys. Res.*, 100, 7423-7440, 1985.

Velden C. S., C. M. Hayden, S. J. Niemann, W. P. Menzel, S. Wanzong, and J. S. Goerss: Winds derived from geostationary satellite moisture channel observations: applications and impact on numerical weather prediction, *Bull. Amer. Meteor. Soc.*, 78, 173-195, 1997.

Vincent, D. G.: The South Pacific Convergence Zone (SPCZ): A review, *Mon. Weather Rev.*, 122, 1949-1970, 1994.

B. J. Soden, Geophysical Fluid Dynamics Laboratory/NOAA, P.O. Box 308, Forrestal Campus, Princeton University, Princeton, NJ 08542. (e-mail: bjs@gfdl.gov)